Determination of Pore Network Accessibility in Hierarchical Porous Solids

Sean P. Rigby[a,*], Muayad Hasan[a,b], Lee Stevens[c], Huw E.L. Williams[d], Robin S. Fletcher[e]

[a]Department of Chemical and Environmental Engineering, University of Nottingham, University Park, Nottingham NG7 2RD, U.K.

[b]Department of Petroleum Technology, University of Technology, Baghdad, Iraq.

[c]Faculty of Engineering, University of Nottingham, University Park, Nottingham NG7 2RD, U.K.

[d]School of Chemistry,Centre for Biomolecular Sciences, University of Nottingham, University Park, Nottingham NG7 2RD, U.K.

[e]Johnson Matthey, P.O. Box 1, Belasis Avenue, Billingham, Cleveland, TS23 1LB, U.K.

* To whom correspondence should be addressed. Email: Sean.Rigby@Nottingham.ac.uk (Tel: +44 (0)115 951 4078)

ABSTRACT

This paper validates the hypothesis that the supposedly non-specific adsorbates nitrogen and argon wet heavy metals differently, and shows how this unexpected effect can be actively utilised to deliver information on pore inter-connectivity. To explore surface chemistry influences on differential adsorbate wetting, new findings for a mixed silica-alumina material were compared with data for pure silica and alumina materials. The new structural characterisation described can determine the distribution of the particular sub-set of meso- and micro-pores that connect directly to macropores that entrap mercury following porosimetry, as mapped by computerised X-ray tomography. Hence, it elucidates the spatial organization of the network and measures the improved accessibility to smaller pores provided by larger pores. It was shown that the silica-alumina pellets have a hierarchical pore-size arrangement, similar to the optimal blood vessel network architecture in animals. The network architecture derived from the new method has been independently validated using complementary gas sorption scanning curves, integrated mercury porosimetry, and NMR cryoporometry. It has also been shown that, rather than hindering interpretation of characterisation data, emergent effects for networks associated with these techniques can be marshalled to enable detailed assessment of the pore structures of complex, disordered solids.

Keywords: adsorbate; wetting; pore network; connectivity; co-operative effects; imaging

1. INTRODUCTION

The development of so-called 'templating'[1] and 'nano-casting'[2] methods to control the void space architecture of mesoporous materials has enabled the concept of designer heterogeneous catalysts, with pore network arrangements optimised for the process conditions applicable to a particular diffusion-limited reaction, to become a potential reality. Recently, hierarchical porous solids have become of particular interest for various applications[3-8]. Computer simulations can predict the likely relative performance of the various potential network architectures[9,10]. A common design proposed to overcome diffusion limitations includes pore networks similar to the tree-like arrangement of passages within the human lung, whereby macropores provide rapid access to the interior, and steadily smaller pores ('lanes') leading off these 'highways' to provide higher surface area for reaction. Various degrees of structural control are possible, depending upon the sophistication, and thence cost, of the synthesis method for the material. Even surfactant-templated materials may contain regions of disorder[1]. Hence, for quality control, the uniformity of manufactured product must be validated to ensure it all has the desired structure. Further, in some reactions the void space of the catalyst pellet may evolve over time due to solids deposition, as in coking[5]. It is thus essential to be able to characterise the spatial arrangement of the various pore sizes, arising from the distribution, as they are juxtaposed relative to each other.

Modern imaging techniques, such as electron tomography (or 3D transmission electron microscopy (TEM))[12], dual-beam scanning electron microscopy (SEM) (or focused ion-beam SEM)[13,14], and computerised X-ray tomography (CXT or CT)[15], can provide full three-dimensional reconstructions of the void space of mesoporous materials at nanometre resolution. However, there is often a limit on the sample size or field of view that can be studied with nanometre-scale resolution. This sampling volume is often much smaller than the correlation length for the local pore structure, or, even if this is not the case, the structure may be macroscopically heterogeneous and thus possess many such similarly-sized regions which each have different void space properties[16]. Hence, direct imaging methods alone cannot provide statistically-representative sampling of the void space of many macroscopic materials. The information thus obtained will, therefore, probably not be sufficient to explain the performance of a full packed or structured bed of catalyst material. There is thus a need for a more representative technique. Economic considerations at the time of writing also favour gas sorption for commercial applications.

Gas adsorption is a long-standing technique that can provide a composite pore size probability density function weighted by pore volume representative of a full macroscopic sample, including up to several catalyst pellets in size. When combined with the corresponding desorption data, percolation theory has been used to interpret the combined data-sets to deliver estimates of pore connectivity[17]. Percolation-based methods necessarily make assumptions about the nature of the spatial correlation of pore sizes, and the typical presumption is of a completely randomised arrangement. However, magnetic resonance imaging (MRI) methods demonstrate the presence of macroscopic heterogeneities (i.e. correlations) in the spatial distribution of porosity, pore size, and tortuosity (related to pore inter-connectivity)[18,19]. The use of gas sorption scanning data does not necessarily improve upon this problem[20]. The information contained in boundary and scanning gas sorption isotherms is insufficient to unambiguously determine pore inter-connectivity alone. Mercury porosimetry can also be used to obtain information of pore neck and body sizes distributions[21,22].

The quantity of information that can be obtained from gas sorption data can be expanded by a combined analysis with mercury porosimetry data[23], or fully integrating sorption experiments with mercury porosimetry conducted on the same sample, whereby they are repeated in series before and after mercury entrapment[24]. These latter experiments can deliver additional information, such as on pore length when combined with percolation theory[25]. The capabilities of single gas sorption can be further expanded upon by combining analysis from multiple adsorbates. Combined analysis of argon and nitrogen adsorption for the same sample has been used to test for cavitation effects in pore size distributions[26]. The combination of several different adsorbates, of different molecular sizes, and percolation theory has been used to determine pore connectivity in microporous solids[27]. However, this method also still relies upon assumptions about pore size spatial correlation. Rather than exploiting variation in adsorbate size, the differences in wetting properties of adsorbates can also be used to expand the information gleaned from adsorption isotherms. The difference in the wetting of mercury by argon and nitrogen has been used to detect the network-based (i.e. pore-pore interaction) delayed condensation effect using integrated porosimetry experiments[14]. This effect has been shown, from simulations on model pore networks, to greatly impact the accuracy of gas sorption pore size distributions[28].

It is the purpose of this work to utilise the different wetting towards mercury surfaces by argon and nitrogen to probe pore size inter-connectivity. The tendency for mercury to become entrapped in the largest pores[29] means that mercury can be used to preferentially fill particular sub-sets of the pore size distribution, such as macroporous 'highways' (or 'motorways'). This creates new mercury surfaces at the junctions of mesopores adjoining macropores containing entrapped mercury, and physically converts the former from through pores to dead-end pores. The higher degree of wetting of the mercury dead-end wall by nitrogen, compared to argon, leads to a significant change in pore potential for nitrogen, but not for argon, which manifests as a shift in condensation pressure. Hence, the specific mesopores neighbouring macropores can be particularly identified by comparing the adsorption of nitrogen and argon within them.

Given the information from the new technique is obtained indirectly, it is important that the description of the void space thereupon obtained is validated. Due to the presence of pore-blocking effects, the freezing curve in NMR cryoporometry can be used to probe pore inter-connectivity[30]. Hence, cryoporometry, gas sorption scanning curves and mercury porosimetry data will be used to validate the new technique, and demonstrate that a void space description can be obtained consistent with data from a range of techniques utilising a number of different physical processes. This is made possible when particular effects, such as snap-off in mercury retraction, and the advanced melting effect in cryoporometry, are taken into account.

2. THEORY

2.1 Mercury porosimetry

While mercury porosimetry data is typically analysed using the Washburn[31] equation, it is well-known[32] that both the surface tension γ and contact angle θ vary with the radius of curvature of the meniscus, and that the contact angle depends upon whether the meniscus is advancing or receding. Hence, previous workers[32,33] have obtained expressions for the term $\gamma.cos\theta$ which take account of these effects. These expressions were obtained from a calibration of the pressure *p*, at which mercury enters or leaves a model porous medium with a relatively ordered structure, against a corresponding, independent measure of pore size *r*,

such as electron microscopy[34]. Insertion of these expressions into the Washburn Equation gives rise to correlations of the form:

$$r = \frac{-A + \sqrt{A^2 - 2pB}}{p} \qquad (1)$$

where *A* and *B* are constants depending on the material, and whether the mercury meniscus is advancing or retreating. The values of *A* and *B* for silica and alumina are given in Table 1. Since the constants in Eq. (1) were derived from empirical methods, they, therefore, have limits to their range of applicability (see Table 1), and also are associated with some experimental error (~4-5 %[32]). However, more recent work[35], using MF-DFT, has now confirmed that the calibration process removes apparent 'contact angle hysteresis' effects.

TABLE 1: Parameters for use in Eq. 1[33]

Material	***A.10*^{3} /(N.m^{-1})**	***B.10*^{12} /N**	**Range of validity /(nm)**
Silica (advancing meniscus)	-302.533	-0.739	6-99.75
Silica (retreating meniscus)	-68.366	-235.561	4-68.5
Alumina (advancing meniscus)	-302.533	-0.739	6-99.75
Alumina (retreating meniscus)	-40	-240	4-68.5

2.2 Thermoporometry

Thermoporometry is possible because the freezing and melting points of a fluid confined to a porous medium are lowered. Typically, the shift in the phase transition point for a small crystal, relative to the bulk, varies inversely with crystal size[36]. When a crystal is melting

within a cylindrical pore, the relevant form of the Gibbs-Thompson equation suggests the melting point depression ΔT_m will be given by:

$$\Delta T_m = T_m^{\infty} - T_m(x) = -\frac{4\sigma_{sl}T_m^{\infty}}{x\Delta H_f \rho_s}cos(\varphi) \quad , \tag{2}$$

where $T_m(x)$ is the melting point in a pore of diameter x, T_m^{∞} is the bulk melting temperature, ΔH_f is the bulk enthalpy of fusion, σ_{sl} is the surface tension, ρ_s is the density of the solid, and ϕ is the contact angle (typically assumed to be 180° for liquid-solid). This equation is often simplified to the form:

$$\Delta T_m = k/x \, , \tag{3}$$

where k is the Gibbs-Thompson constant. In previous work[37], it has been found that for melting of a mercury crystal via a hemispherical meniscus, the value of k is 90 nm K.

Borisov *et al.*[38] found that a thin liquid-like layer forms on the surface of confined, solid mercury ganglia over the temperature range 195 to 229 K. This liquid-like layer forms the initiating site for melting of the solid cores at a higher temperature, depending on characteristic size. It is thought that this liquid-like layer is one molecular diameter thick, and, hence, the effective crystal size in eq 3 becomes x-t, where t is the thickness of the liquid-like layer.

2.3 Integrated experiments and surface wetting effects

The integrated experiment consists of a series of gas sorption and mercury porosimetry runs conducted in series on the same sample, with the entrapped mercury frozen in place before the next gas sorption experiment is commenced. The stages of the experiment are shown schematically in Figure 1.

Figure 1. Schematic diagram of integrated gas sorption and mercury porosimetry experiment in a generic pore space. The stages of the experiment are: (1) Empty sample; (2) First gas sorption experiment; (3) Empty sample; (4) Hg porosimetry; (5) Hg entrapment; (6) Second gas sorption experiment. Reprinted from Journal of Colloid and Interface Science, 417, Iain Hitchcock, Marie Lunel, Serafim Bakalis, Robin Fletcher, Elizabeth Holt and Sean P. Rigby, Improving sensitivity and accuracy of pore structural characterisation using scanning curves in integrated gas sorption and mercury porosimetry experiments, 88-99, Copyright (2014), with permission from Elsevier.

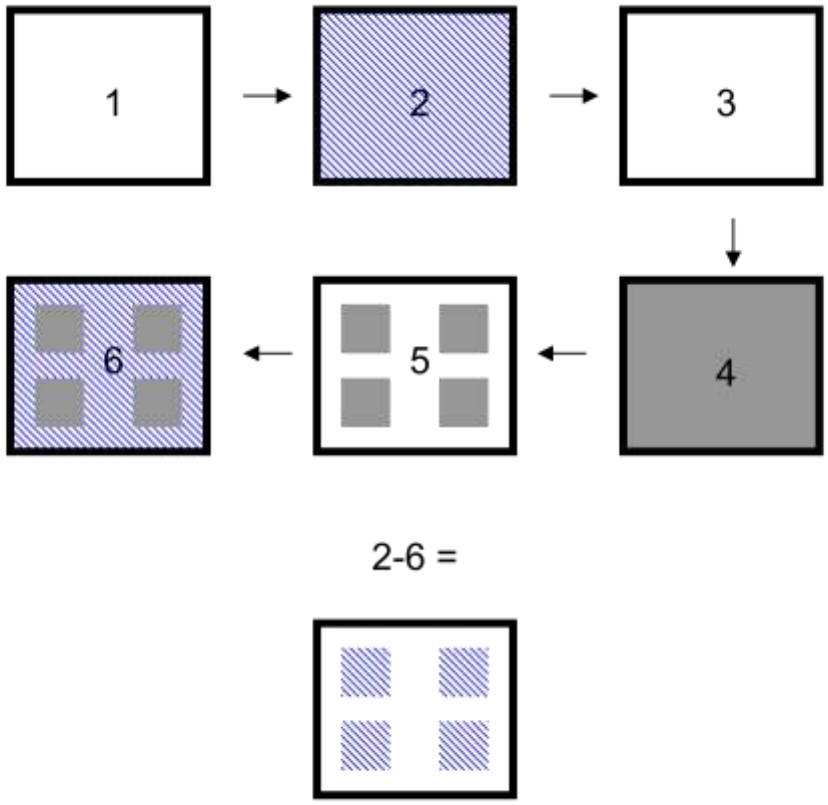

The isotherm obtained in stage 6 of the integrated experiment depends upon whether the adsorbate wets the new mercury surfaces formed following entrapment. Previous work[14] suggested that, while both argon and nitrogen are excluded from pores that contain entrapped mercury, only nitrogen substantially wets the new mercury surfaces formed at the intersections of empty pores with newly-filled pores. It has been shown previously[39] that, while the surface fractal dimension derived from the adsorption isotherm decreased after mercury entrapment in a mesoporous silica when nitrogen was used as the adsorbate, there was no such statistically significant variation in fractal dimension when argon was used as the adsorbate. It was proposed that this difference in findings arose because nitrogen wetted the smooth mercury metal surface similarly to silica, while argon preferentially wetted silica relative to mercury. Hence, when mercury entrapment created free metal surfaces, the

nitrogen multi-layer film readily extended over these surfaces, but the adsorption of the argon multi-layer film remained relatively more localised upon the silica surface for relative pressures in the usual multi-layer range. Since a mercury metal surface is flat, but an amorphous silica surface is rough, then the creation of mercury surfaces within a sample with entrapment would be expected to decrease the apparent surface fractal dimension characterising the overall roughness for an adsorbate that also wets the mercury. This is just what was observed for nitrogen, in contrast to argon, adsorption for sol-gel silicas in previous work[39]. However, the fractal dimension did decline significantly for both nitrogen *and* argon following mercury entrapment in an alumina sample, which suggested that the wetting of alumina and frozen mercury was relatively similar for both adsorbates[39]. This begs the question concerning what will happen for a sample containing both silica and alumina.

In the case of a sample where the mercury becomes entrapped solely in macropores, that connect to a sub-set of the micro- and meso-porosity, the anticipated findings of an integrated experiment for nitrogen and argon are shown schematically in Figure 2. Following entrapment, a through mesopore, which connected to a macropore that becomes filled with entrapped mercury but retained access to the exterior, is turned into a dead-end pore for nitrogen, but not for argon. This change would result in a lowering of the condensation pressure for nitrogen, but not for argon. Figure 2 shows these effects on the observed incremental adsorption for such a through mesopore, and also the effect of entrapment on observed incremental adsorption for another, smaller pore that only has access to the exterior via the macropore that becomes filled with entrapped mercury. Also shown in Figure 2, is the anticipated cumulative difference in amount adsorbed plots for nitrogen and argon for a system containing a distribution in meso- and micro-pores that connect to the macroporosity, in one of the two ways described above.

Figure 2. Schematic diagram illustrating (a) the behaviour of the menisci at the pore scale and (b) the findings anticipated for the adsorption levels in different pores for integrated experiments with either nitrogen or argon.

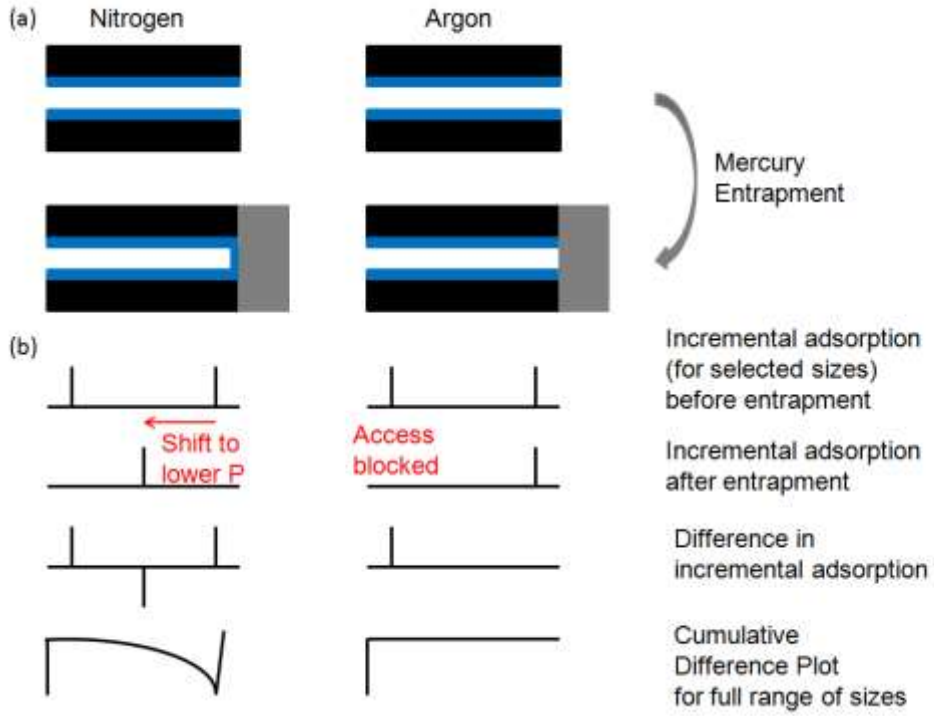

3. MATERIALS AND METHODS

3.1 Material

The material under test was a silica-alumina process catalyst. The results for the five most common elements emerging from the elemental analysis of the material are shown in Table 2. The balance of the composition is made up of trace metals, such as potassium and tin, and oxygen. It can be seen from Table 2, that the catalyst is predominantly a mixture of silica and alumina. Figure 3 shows CXT images of radial plane and axial plane cross-sections of a typical sample of the silica-alumina catalyst. The dark, worm-like forms in the image are macropores within the body of the pellet. Given that the macroscopic spatial distribution of macroporosity in the CXT images is not uniform, it can be seen that a technique that permits macroscopic sampling of the fraction and type of mesopores directly accessible from the macropores would be important for this material.

Table 2. Elemental abundance for most common elements in silica-alumina material.

Element	**Amount/ wt.%**	**Amount/ at.%**
Al	37.45	40.54
Si	46.58	48.44
Cl	7.52	6.20
Ti	4.97	3.03
Fe	2.20	1.15

Figure 3. (a) radial plane and (b) axial plane CXT images of typical cross-sections through a sample of silica-alumina Pellet. The lightest gray-level corresponds to highest density, and dark regions correspond to porosity. The scale bar corresponds to 1000 μm.

(a)

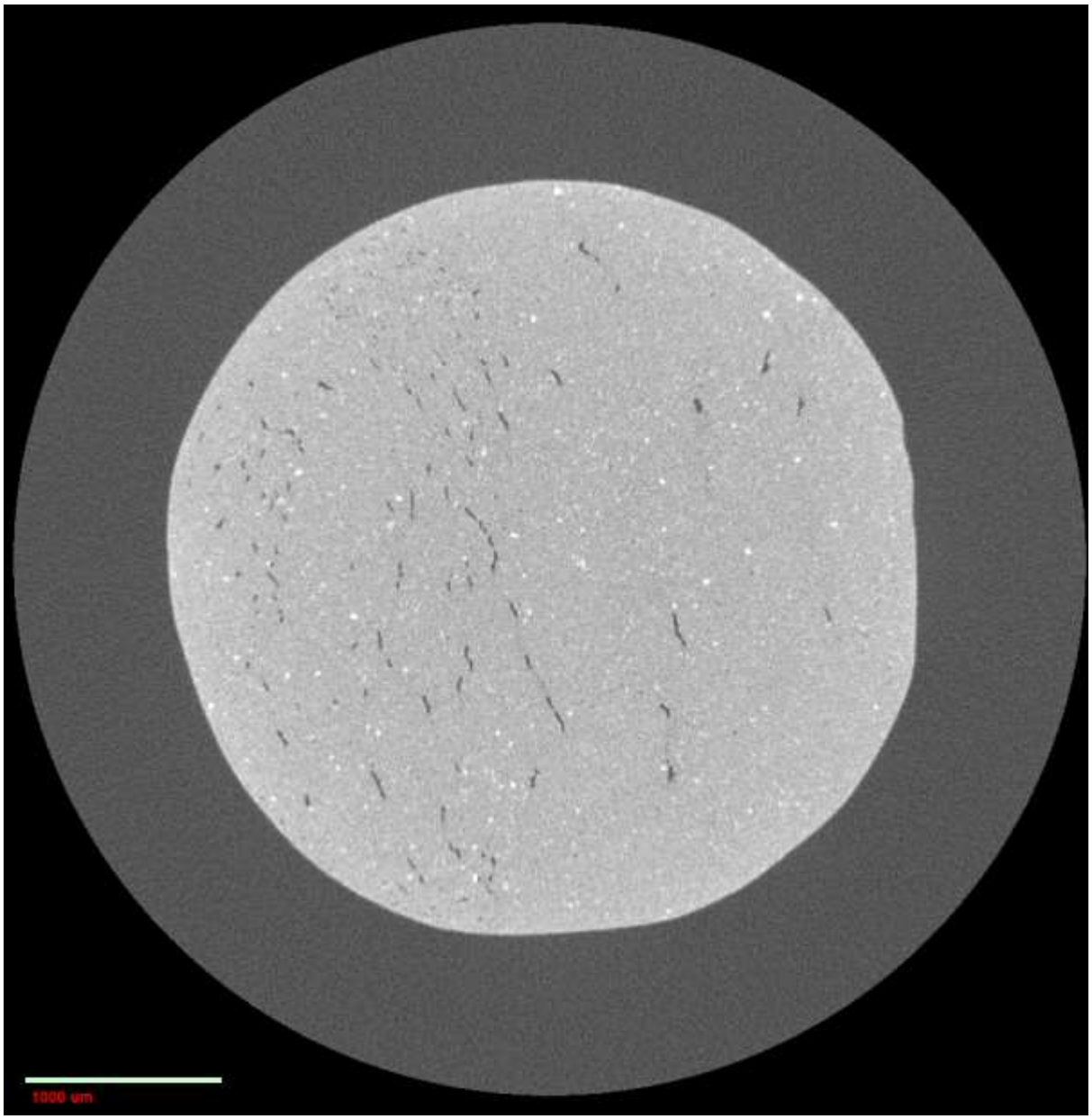

(b)

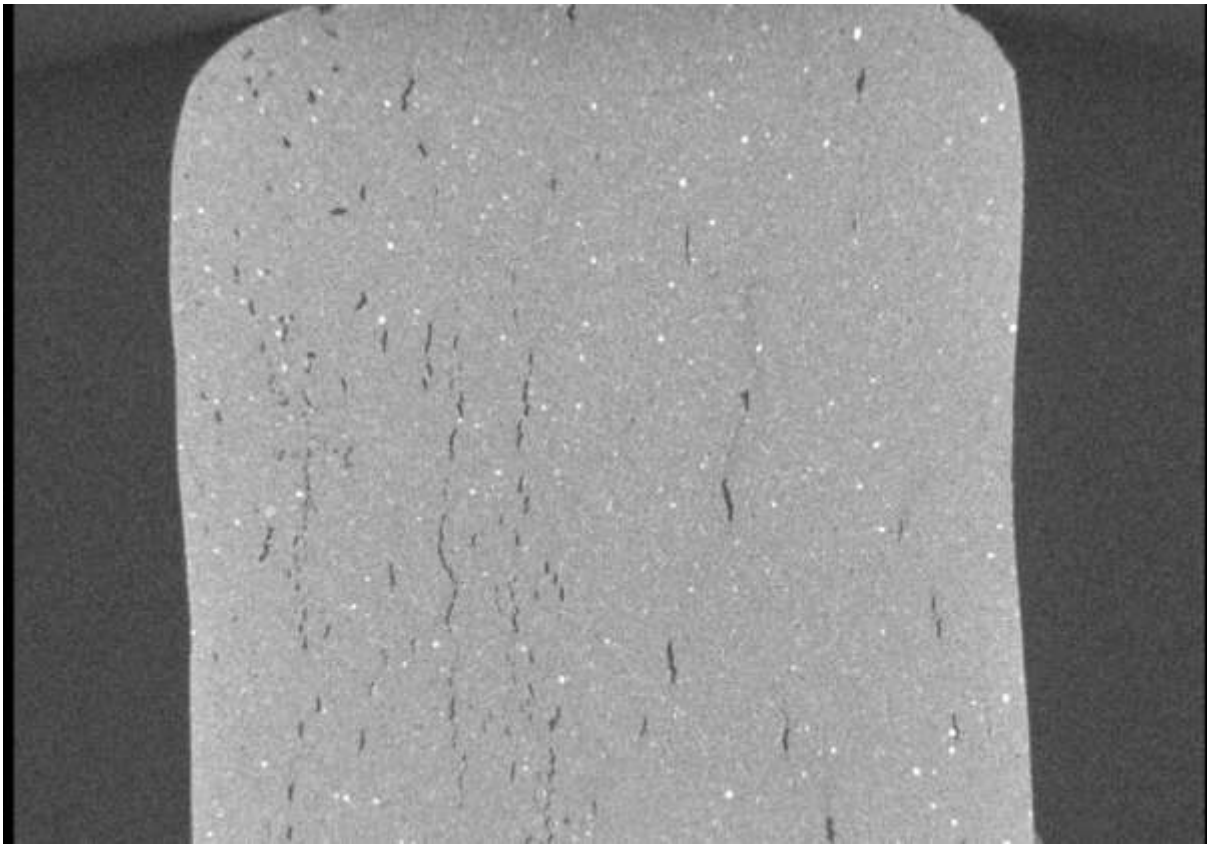

3.2 Computerised X-ray tomography (CXT)

The sample before and following mercury porosimetry was imaged using a High Resolution X-ray 3D Computed Tomography Microscope Instrument of model VeraXRM-510 (manufactured by Xradia Inc, Pleasanton, CA, USA). The voxel resolution was 5.5 μm. Typically 2-3 pellets of each sample type were imaged.

3.3 Integrated gas sorption and mercury porosimetry

The basic procedures for the sample preparation and integrated gas sorption experiments have been described in detail previously[14], and, thus, only key aspects will be mentioned here. A Micromeritics Accelerated Surface Area and Porosimetry (ASAP) 2020 apparatus was used for the nitrogen sorption experiments at 77 K, and a Micromeritics 3500 3Flex, fitted with a Cold Edge Cryostat to cool the sample to 87 K, was used for argon sorption experiments. Mercury Intrusion Porosimetry was carried out using a Micromeritics AutoPore 9520. The

equilibration time used for porosimetry experiments was 15 s, as sensitivity studies had shown this value leads to a fully equilibrated intrusion curve.

In previous work[39] it was shown that the surface fractal dimensions (see below) for silica surfaces derived from argon adsorption isotherms following mercury entrapment were identical to those obtained independently from SAXS. This finding showed that adsorption following entrapment was not being impacted by contamination due to films of condensed atmospheric moisture that might have formed during transfer of the sample between the two different sets of apparatus utilised in the integrated experiment.

3.4 Mercury thermoporometry

Pellet samples for the thermoporometry experiments were prepared using mercury porosimetry. The DSC experiments were carried out employing a DSC Q10 V9.8 apparatus, and generally according to the method described in detail in Bafarawa *et al.*[37] except where stated here. First, the sample with entrapped mercury was frozen in the DSC cell at a temperature of -80 $^{\circ}$C, and then this temperature was kept fixed for 30 minutes to ensure thermal homogeneity. The melting curves were obtained for the temperature range from -80 $^{\circ}$C to -37 $^{\circ}$C at the low scanning rate of 0.5 $^{\circ}$C min^{-1}. Preliminary sensitivity studies had established this rate was the most appropriate. The DSC has the capability to measure heat flow rates with a resolution of ±0.5μW and an accuracy of ±2μW.

3.5 NMR cryoporometry

Experiments were conducted on a Bruker Avance III 600 MHz spectrometer. For the cryoporometry melting curve experiments, the sample was pre-soaked in water to complete saturation, and then the confined water was super-cooled to 235 K, and the sample was warmed up in steps of 0.3 K per 10 minutes. The NMR spectrum was taken at each temperature following equilibration. Data were acquired using an echo filter and the echo time was chosen such that no signal was obtained when the sample was fully frozen. Freezing scanning curves were also performed where the sample melting was halted before the ice in the macroporosity and bulk phase had melted, and freezing re-commenced.

4. RESULTS

4.1 Integrated gas sorption and mercury porosimetry

Figures 4 and 5 show the nitrogen and argon sorption isotherms obtained before and after mercury entrapment following a mercury porosimetry experiment. In the cases of both adsorbates, the amount adsorbed drops significantly following mercury entrapment.

Figure 4. Nitrogen adsorption (+ after porosimetry; ◇before porosimetry) and desorption (× after porosimetry; ☐ before porosimetry) isotherms conducted at 77 K for a typical sample of silica-alumina catalyst.

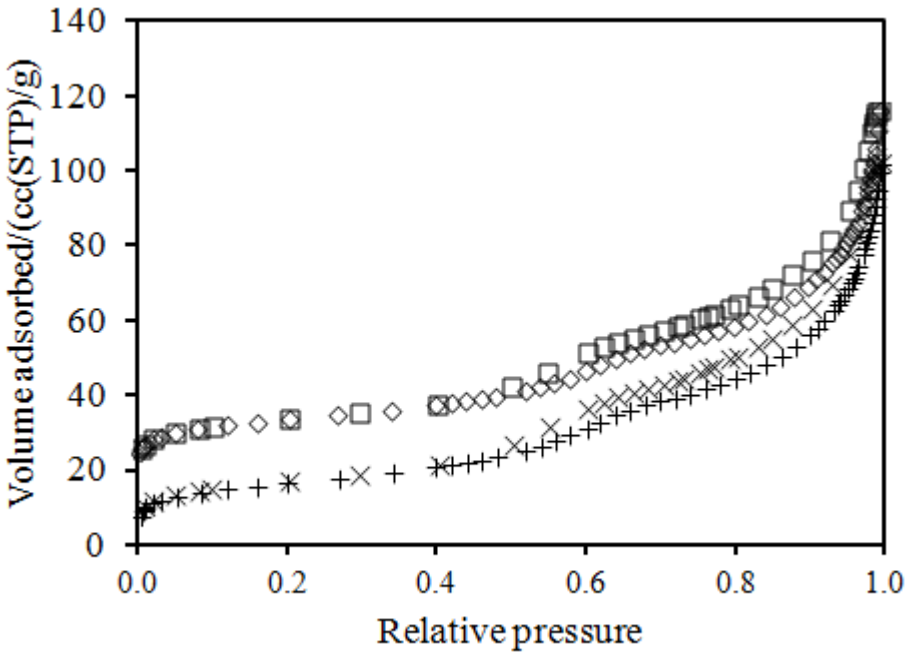

Figure 5. Argon adsorption (+ after porosimetry; ◇before porosimetry) and desorption (× after porosimetry; □ before porosimetry) isotherms conducted at 87 K for a typical sample of silica-alumina catalyst.

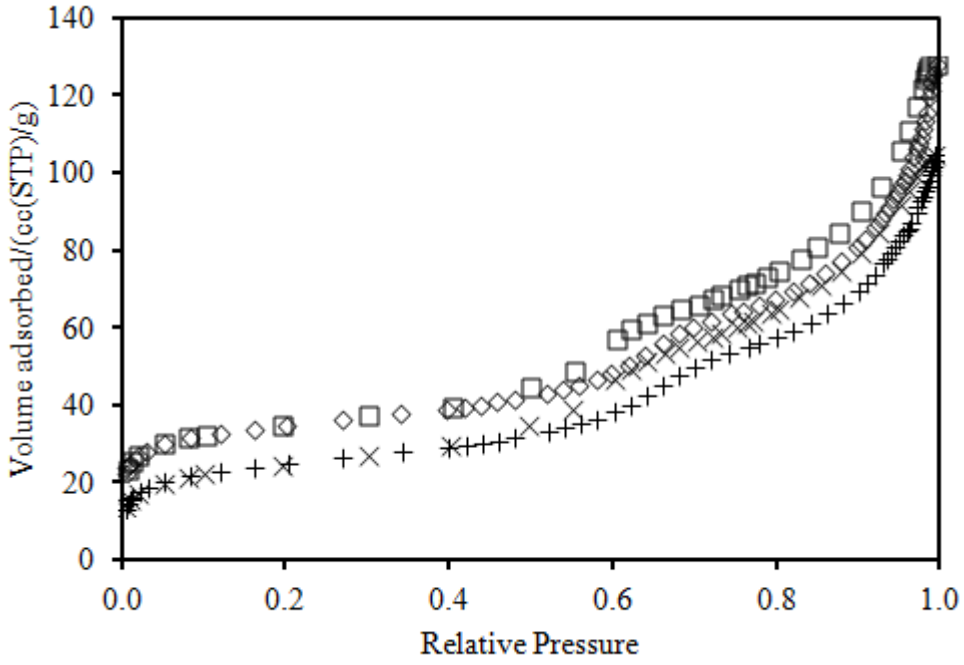

Figure 6(a) shows the cumulative difference in amount adsorbed plots obtained from subtracting the isotherm obtained after porosimetry from the one before porosimetry. From Figure 6(a) it can be seen that, while the plot for argon is generally flat over a wide range of relative pressure after the micropore region, the cumulative difference in amount adsorbed for nitrogen is generally declining at relative pressures beyond the multi-layer region, and the steepness of that decline generally is increasing with relative pressure, apart from a brief hiatus around 0.6. At the very highest relative pressures, close to one, the nitrogen curve begins to rise steeply like the argon curve. Between relative pressures of ~0.62-0.68 there is a small peak in the argon cumulative difference plot, while in the corresponding spot in the nitrogen plot there is a flat plateau. The peak in the argon data implies that there is a small volume of the void space for which the condensation pressure has increased slightly following entrapment, but this was not the case for nitrogen at the same relative pressure. The position of the peak is close to the relative pressure where there is a kink in the boundary adsorption isotherms for both gases. The pore diameter at this kink is ~6.2 nm by the Kelvin equation or NLDFT for nitrogen.

Figure 6(b) shows the histogram of the distribution, weighted by volume, of the sizes of pores within which capillary condensation was affected by the mercury entrapment, which was derived from the nitrogen data given in Figure 6(a). Hence, this represents the distribution of pores which have been converted from through-pores, initially connected to the macroporosity, to dead-end pores by entrapment. It can be seen that the largest peak corresponds to the largest pore sizes.

Figure 6. (a) Cumulative difference in amount adsorbed between gas adsorption isotherms obtained before and after mercury entrapment for nitrogen (×) and argon (+) on silica-alumina catalyst. (b) Distribution of pore sizes where condensation was impacted by mercury entrapment.

(a)

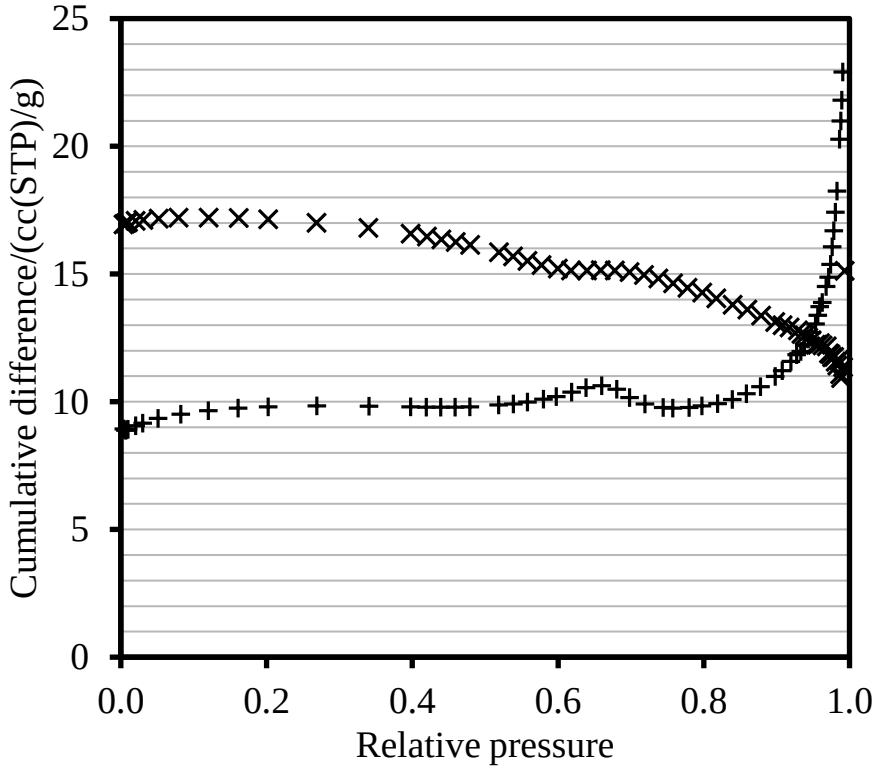

(b)

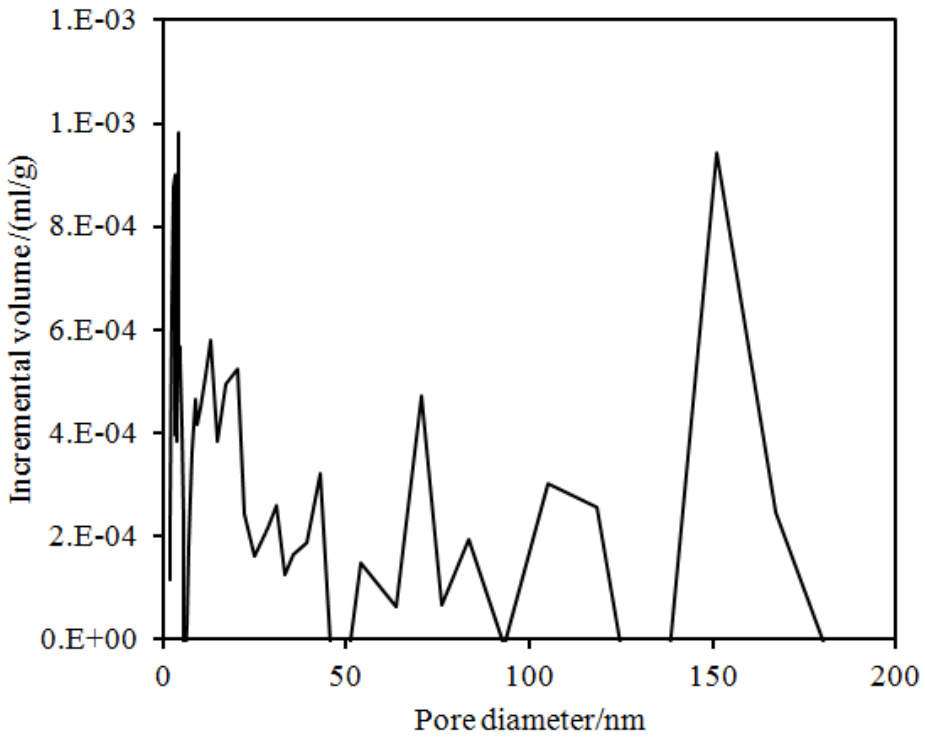

The multi-layer adsorption region of the argon adsorption isotherm obtained before mercury entrapment was fitted to a homotattic patch isotherm model[40], consisting of patches obeying either a Langmuir or a fractal BET isotherm[35]. This model was chosen because of the micropore filling occurring at low pressure, obvious from the isotherm shape, which showed a steep uptake at low pressure. The surface fractal dimension of the mesoporosity thereby obtained from the fractal BET component for the silica-alumina catalyst was 2.07±0.01.

In addition to the full boundary isotherms a series of nitrogen scanning curves were also obtained for the silica-alumina catalyst, and these are shown in Figure 7. From Figure 7, it can be seen that the boundary adsorption and desorption isotherms had a pronounced kink at relative pressures of 0.66 and 0.60, respectively. Scanning curves were conducted up to these ultimate relative pressures and the higher relative pressures of 0.85 and 0.90. From Figure 7(a) it can be seen that while the scanning curve to a relative pressure of 0.60 on the adsorption branch descends to the lower closure point of the hysteresis, the scanning curve to a relative pressure of 0.66 on the adsorption branch crosses directly to the boundary

desorption curve. From Figure 7(b) it can be seen that, for all of the scanning curves to relative pressures above 0.66 on the adsorption branch, they descend to the kink in the desorption boundary curve at a relative pressure of 0.60 as if it were the lower closure point of a hysteresis loop.

Figure 7. (a) Nitrogen sorption scanning curves up to relative pressures of 0.6 (+ and dotted line) and 0.66 (× and solid line), and boundary curves (dashed line and dot-dash line). (b) Nitrogen sorption scanning curves up to relative pressures of 0.85 (+ and dotted line) and 0.90 (× and solid line), and boundary curves (dot-dash line and dot-dot-dash line).

(a)

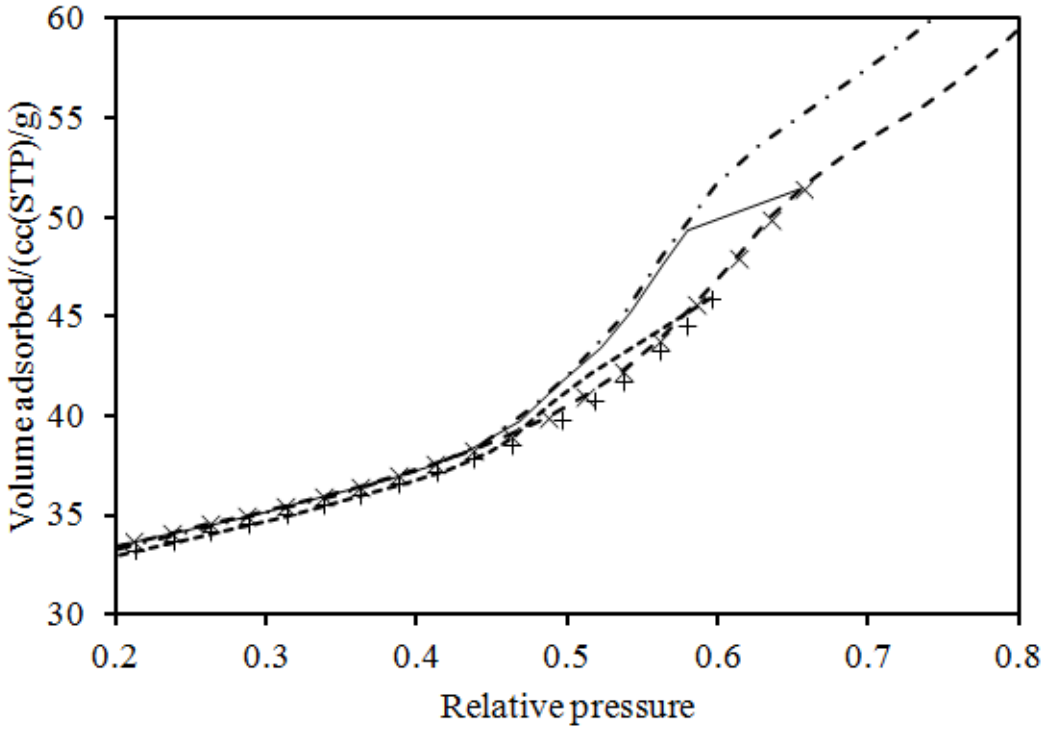

(b)

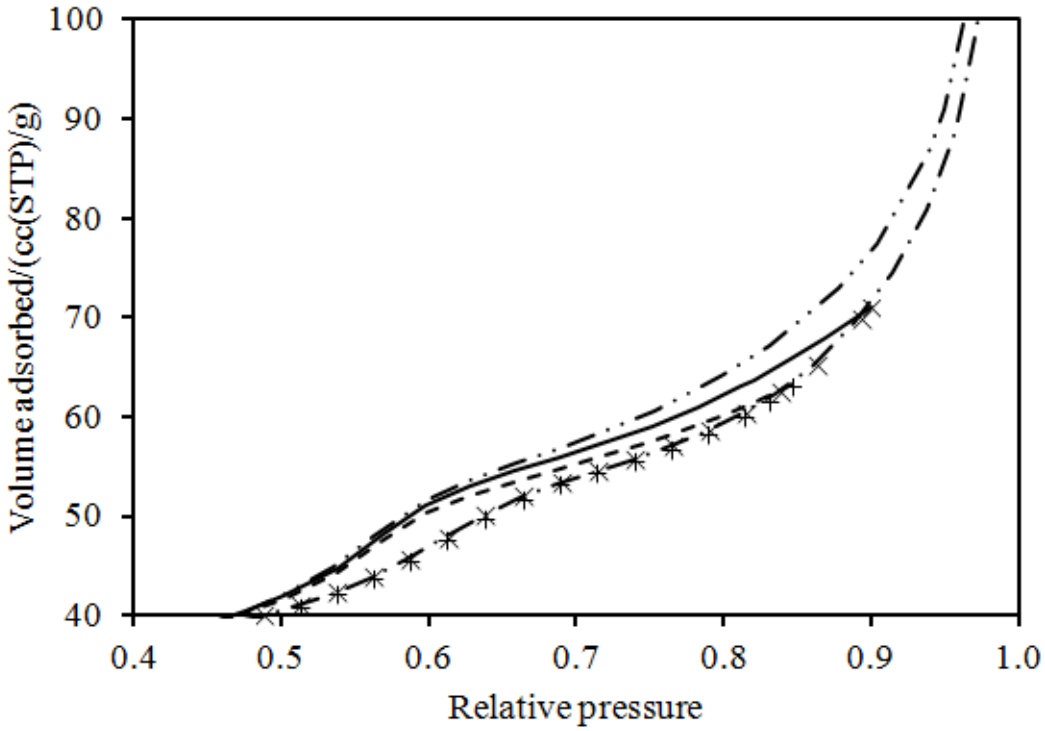

Figure 8 shows a typical example of the raw data obtained from the intermediate mercury porosimetry for an integrated experiment with gas sorption. Since the surface fractal dimension obtained above for the silica-alumina material was similar to that for the controlled pore glasses (CPGs) used to calibrate the Washburn equation by Kloubek[32], then the data was analysed using the standard Kloubek[32] correlation parameters (Table 1) for the surface tension and contact angle equation in the Washburn equation (Figure 8(b))[35].

Figure 8. (a) Raw mercury porosimetry data for silica-alumina catalyst. (b) Data from (a) with inter-particle intrusion deducted and analysed using Kloubek[32] correlations (eq. 1 and Table 1).

(a)

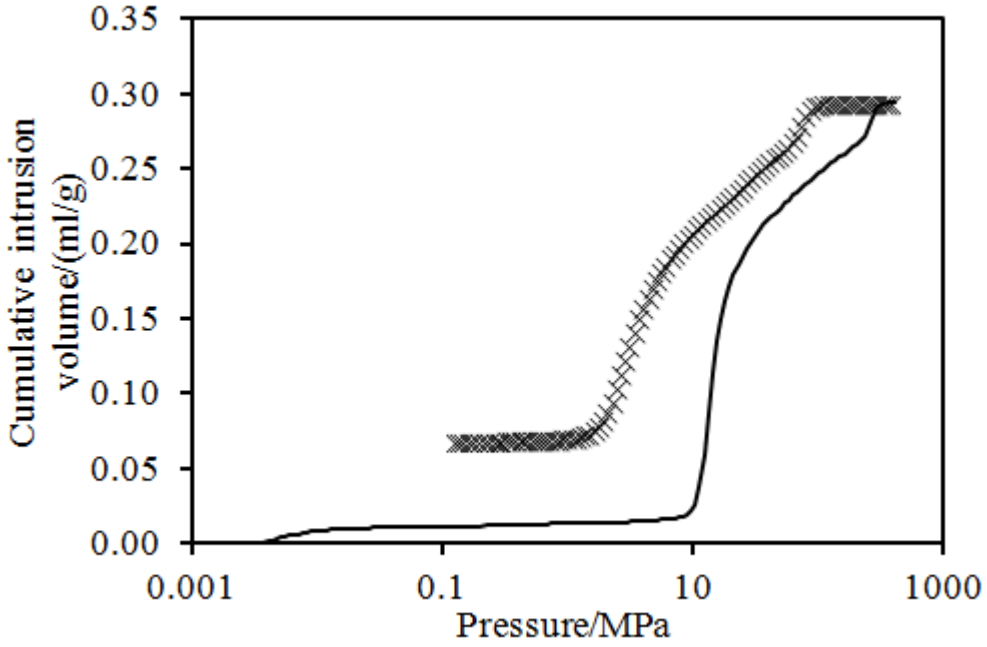

(b)

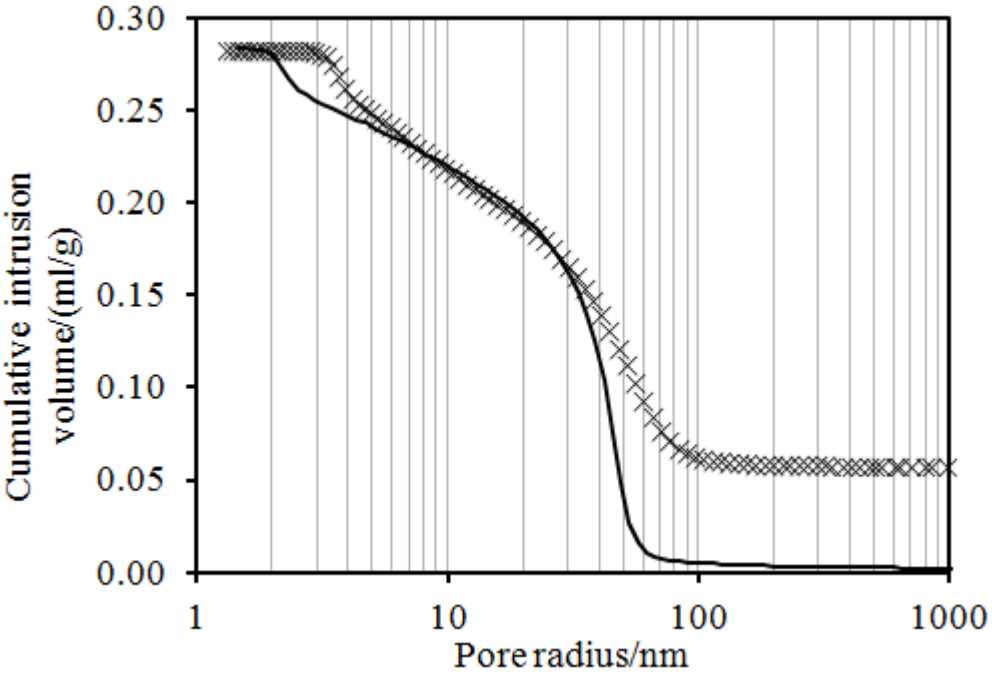

From Figure 8(b) it can be seen that the Kloubek[32] correlations lead to the superposition, within experimental error, of the intrusion and extrusion curves at intermediate pore sizes in the range of radii from ~7-30 nm. The pore sizes for the smallest mode in the mercury intrusion curve correspond to those below the kink in the nitrogen adsorption isotherm data. The top of the intrusion curve has a flat plateau suggesting that mercury has completely filled the mesopore network. The initial part of the retraction curve is also flat, indicating no mercury is extruded until the sharp first step, and so there is some hysteresis retained even after the removal of the contact angle contribution via the application of the Kloubek[32] correlations. The amount of mercury retracting from the sample is less than that which originally intruded for intrusion pore radii in the range ~30-100 nm, thereby suggesting mercury is entrapped within the largest pores.

4.2 CXT

Figure 9 shows CXT images of radial cross-sections through a sample of silica-alumina catalyst following mercury porosimetry. The brightest white pixels are regions with the largest X-ray absorbance and correspond to mercury-filled regions. It can be seen that the mercury occupies isolated, macroscopic-sized regions that are similar in typical form and distribution to the previously low X-ray absorbing macropores seen in Figure 3. Hence, the images suggest that mercury becomes entrapped in the pellet macroporosity.

Figure 9. Images of radial cross-sections from a typical sample of Silica-alumina catalyst following mercury porosimetry. The brightest white pixels correspond to the highest density mercury-filled macroporosity and the mid-grey pixels correspond to solid matrix. The scale bar corresponds to 1000 μm.

(a)

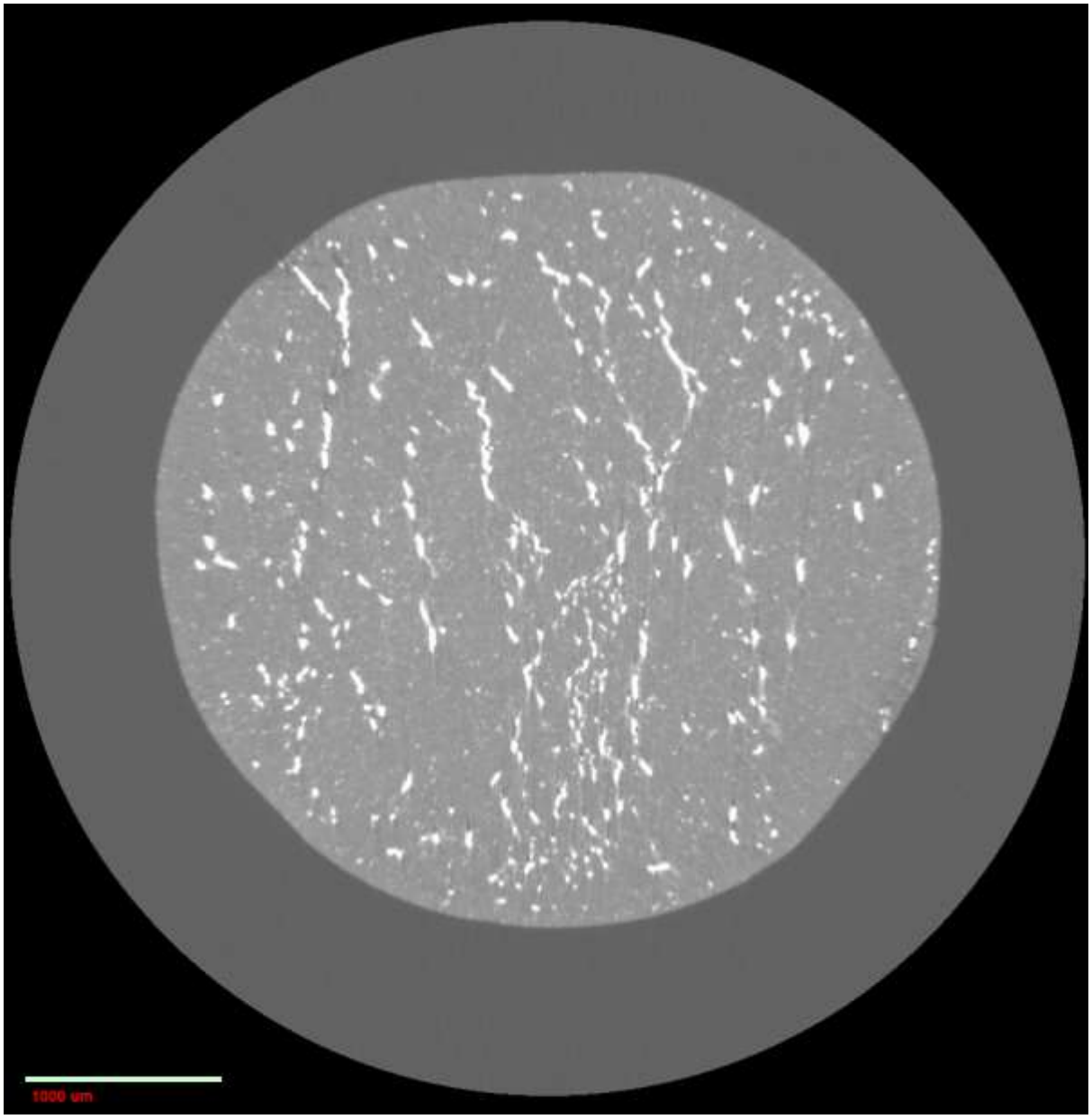

(b)

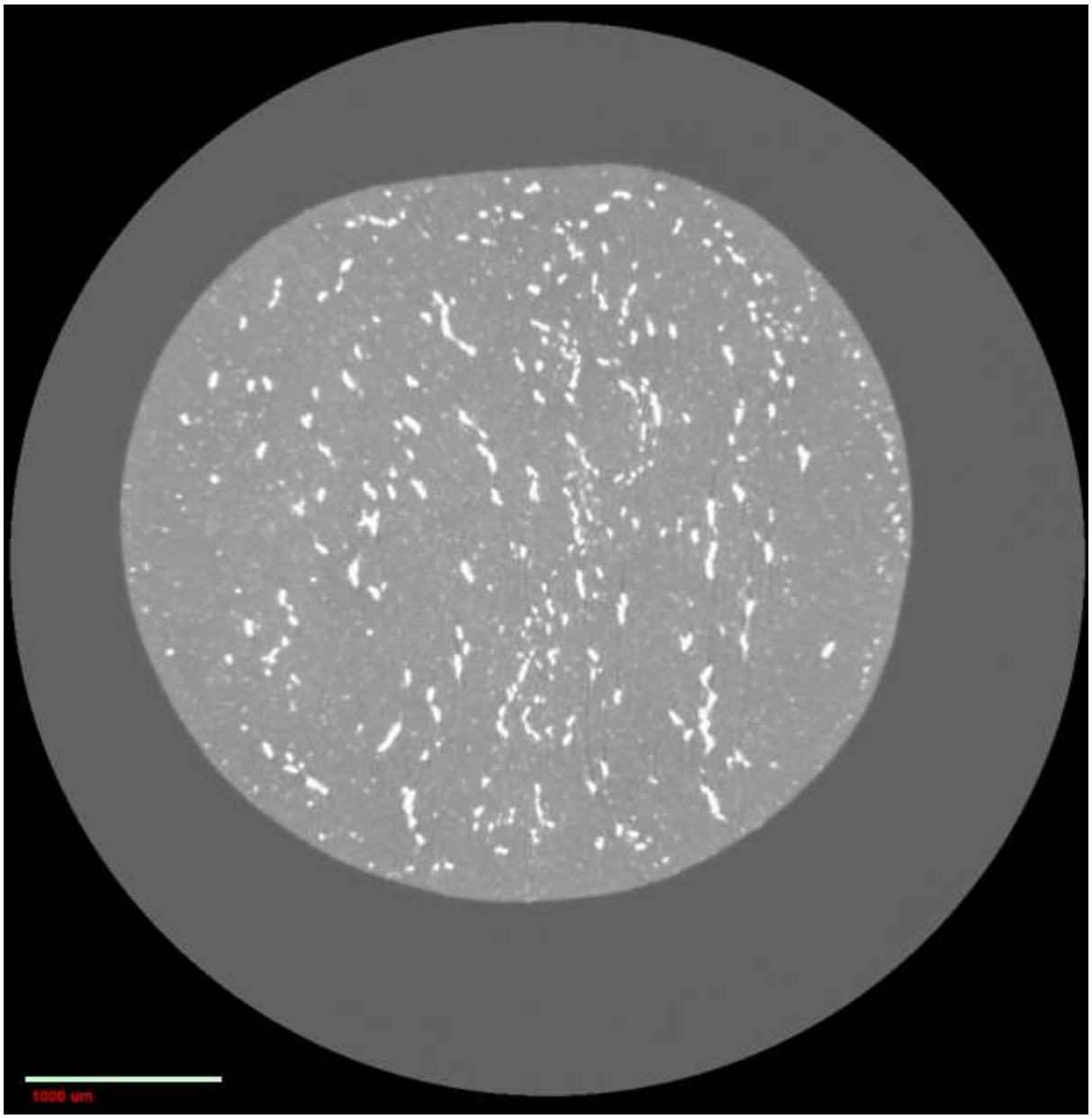

4.3 Mercury Thermoporometry

Figure 10 shows the DSC thermoporometry melting curve for a sample of silica-alumina catalyst following mercury porosimetry. The bulk melting temperature for mercury is -38.8 $^{\circ}$C. The position of the melting peak in the DSC data at ~ -39.5 $^{\circ}$C, and the Gibbs-Thompson parameter for mercury mentioned in the Theory section, suggests that entrapped mercury is present as ganglia in the macroporous size range. While the closeness of the mercury melting point to the bulk value, without doubt, suggests very large mercury ganglia sizes, the resulting very small melting point depression makes precision difficult given there will be

error (±0.3 °C) in the temperature measurement similar in order to the observed depression. However, this data confirms the suggestion from the CXT data that entrapped mercury is confined to the pellet macroporosity.

Figure 10. DSC thermoporometry melting curve for a sample of silica-alumina catalyst following mercury porosimetry.

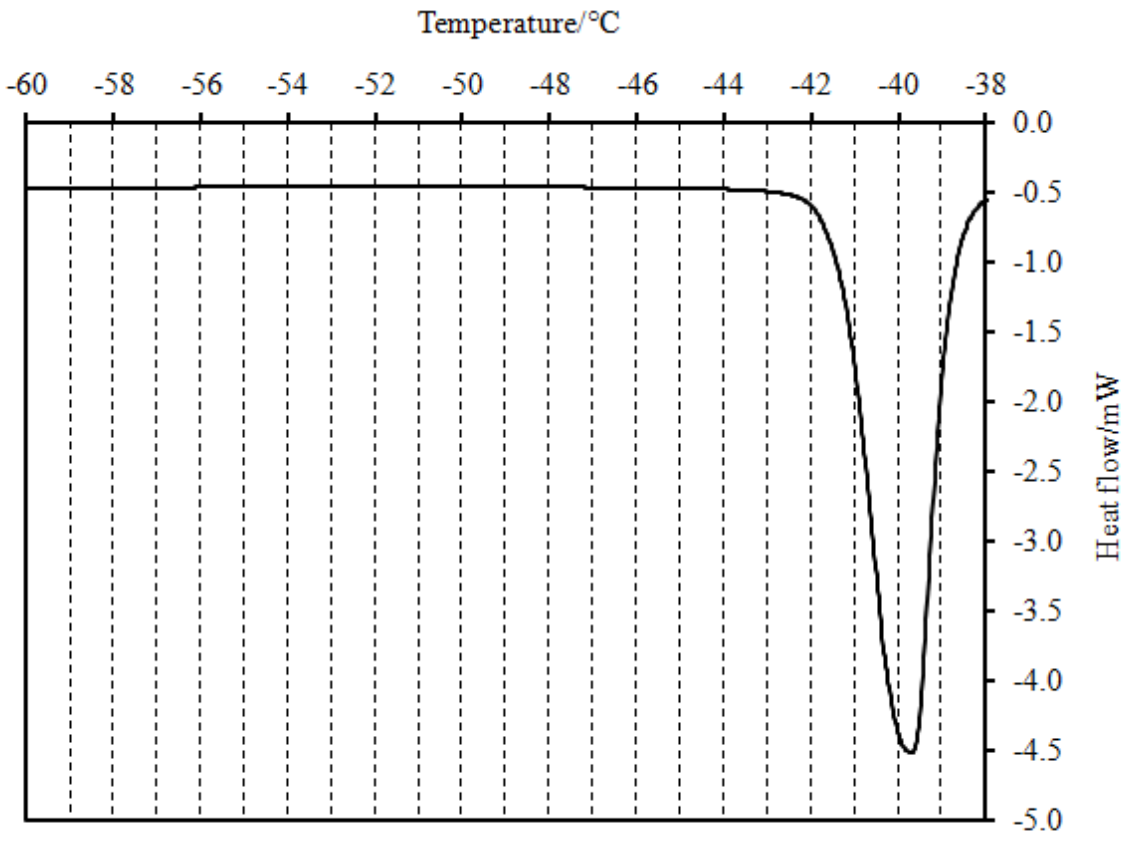

4.4 NMR cryoporometry

Figure 11 shows the NMR cryoporometry boundary melting curves for bulk ice and water imbibed within the void space of the silica-alumina catalyst. It can be seen that the melting temperature is depressed for the water in the void space of the sample. Figure 11 also shows a melting-freezing scanning curve up to an ultimate temperature of 272 K. It is noted that the hysteresis between the melting and freezing branches of the scanning curve is initially (around the point where the temperature rise is reversed) very narrow, being perhaps only ~0.5 K, and stays very narrow until a temperature of ~269 K, but by a melting temperature of

267 K the hysteresis width has grown to ~6 K. Hence, at a temperature of 267 K the freezing point depression is about twice that of the melting point depression. For a Gibbs-Thompson parameter of 52 K nm (for melting from a cylindrical sleeve meniscus) and non-melting layer thickness of 0.4 nm, calibrated using templated mesoporous silicas[36] the pore diameter at this point is ~9.4 nm. This corresponds to the bottom end of the residual hysteresis loop retained in the mercury porosimetry data analysed using the Kloubek[32] correlations shown in Figure 8(b).

Figure 11. NMR cryoporometry boundary melting curves for bulk ice (solid line) and water imbibed within the void space of the silica-alumina catalyst (dashed line). Also shown in a melting-freezing scanning curve (× and dotted line) up to 272 K. The double-headed arrow indicates that the width of the hysteresis between the freezing and melting branches of the scanning curve has grown to ~6 K at a melting temperature of 267 K.

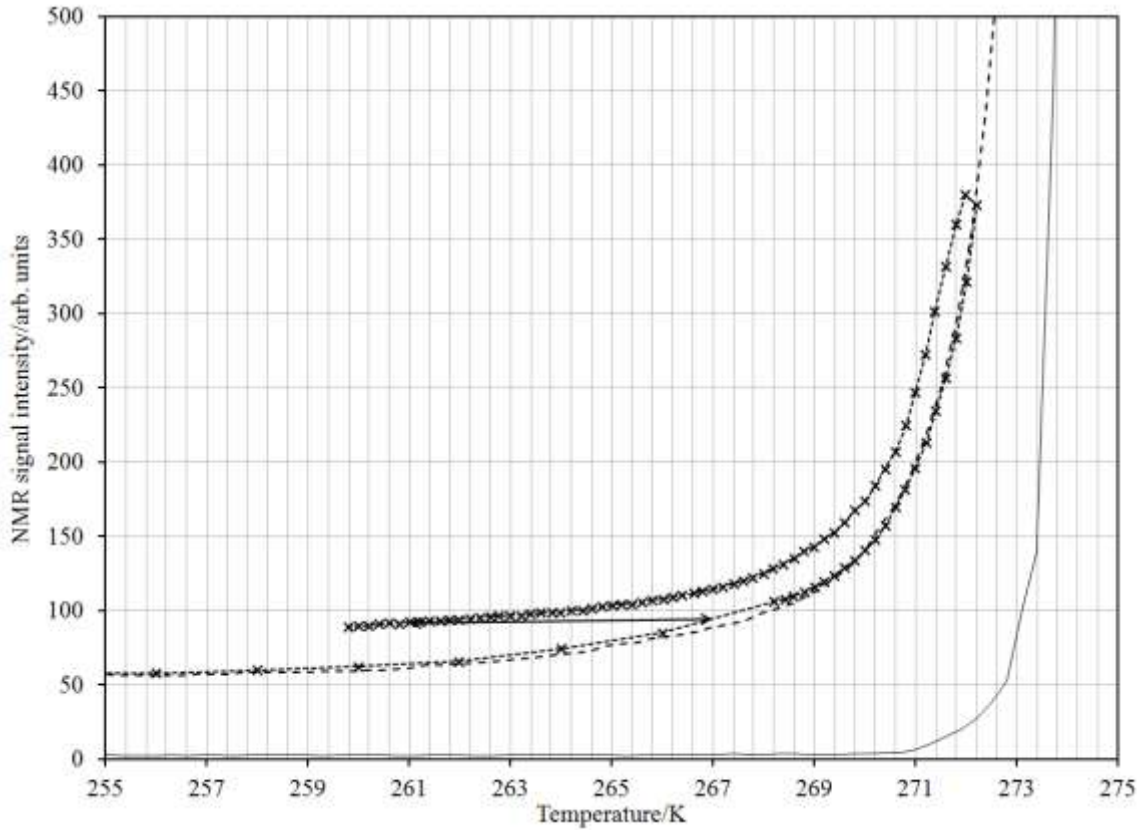

5. DISCUSSION

It has been seen that the CXT and mercury DSC thermoporometry data for the silica-alumina catalyst suggests that the mercury entrapment during porosimetry is restricted to the very

largest macropores in the sample. However, it is clear from the difference in the amount adsorbed plots in Figure 6 that capillary condensation occurring at relative pressures corresponding to pore sizes in the mesopore range are affected by mercury entrapment. Hence, the entrapped mercury affects capillary condensation occurring in the smaller, still open pores adjacent to it. The forms of the cumulative difference in amount adsorbed plots for nitrogen and argon have been found to be consistent with the scenario described in the above Theory section. The entrapped mercury in the macropores creates dead-ends at their junctions with the previously open, through pores. The new mercury dead-ends lead to a reduction in the capillary condensation pressure for nitrogen, as might be anticipated from the Cohan[42] equations. However, argon is much less wetting of the entrapped mercury, relative to the silica-alumina surface, and, thus, the pores with mercury dead-ends still behave like through pores for argon. Hence, nitrogen and argon behave in this silica-alumina material similarly to the pure silica materials, rather than the pure alumina, studied previously[14,39]. The initial high value of the cumulative difference plots at the lowest relative pressures for both nitrogen and argon is because both adsorbates are being excluded from the microporosity that fills at low pressure. This suggests that the microporosity that fills at the lowest pressure is accessible only via the largest macropores that get filled with entrapped mercury, as shown in Figure 12. This suggests that the microporosity is probably surface roughness of the macropores. The micropores are too small to fill with mercury at the top of the mercury intrusion curve.

The mercury porosimetry, nitrogen sorption scanning curves and NMR cryoporometry scanning curve data are all consistent with the schematic model of the pore network given in Figure 12. The retention of the hysteresis between the intrusion and extrusion curves at the highest pressures after the raw data had been analysed using the Kloubek correlations suggested an additional source of hysteresis beyond contact angle variation. The flat plateau at the top of the intrusion curve suggested that all of the mesoporosity had been filled with mercury and that it is therefore likely that all the mercury menisci in the mesopores would have coalesced. This means that for retraction to commence a new pair of menisci would need to be generated by the ‘snap-off’ process[43]. The residual hysteresis arises because the mercury pressure must be reduced sufficiently to generate the free menisci. The triangular shape of the hysteresis region at high pressure in the experimental data above is consistent with what has been observed in mean-field density functional theory (MF-DFT) simulations of intrusion and retraction in pore networks consisting of small pores forming through

bridges between larger pores[35]. The snap-off process is initiated in the small through-pore. Sometimes snap-off can occur multiple times in the same pore bond thereby leaving a small amount of mercury stranded. A rare occurrence of this may have led to the small positive peak, at relative pressures ~0.62-0.68, in the argon cumulative difference in amount adsorbed plot (Figure 6(a)). If a small amount of mercury became entrapped in the neck, where the smallest pores join the medium pores in Figure 12, then the non-wetting surface for argon thereby created may have led to an increase in the argon condensation pressure for neighbouring medium-sized pores, while the nitrogen condensation would be unaffected.

The transition between descending, then crossing, and back to descending gas desorption scanning curves observed for the silica-alumina catalyst is also consistent with the pore model shown on Figure 12. The filling process for the highly-simplified, model network shown in Figure 12 would commence with capillary condensation via the cylindrical sleeve-shaped meniscus within the smallest through pores. If at the ultimate highest pressure of the scanning curve, the smallest through pores were filled with liquid condensate but the other larger pores were left empty, then desorption from the smallest pores would commence from the hemispherical menisci at the junctions of the smallest pores and the other larger pores. According to the Cohan equations, this would result in wide hysteresis, and, thence, a crossing scanning curve. This is what is observed for scanning curves turning around at the kink at relative pressure of 0.66 in the boundary adsorption isotherm. Once the smallest pores in the model are full of condensate, the medium pores can potentially fill by advanced condensation from the hemispherical meniscus formed at the ends of the smallest pores. If at the ultimate highest pressure of a scanning curve, the smallest and medium pores are filled with liquid condensate, but the largest macropores are left empty, then desorption from the filled pores will commence from the hemispherical menisci at the junctions of the medium pores and the largest macropores. Hence, given the meniscus geometry is the same for adsorption and desorption then no hysteresis would be anticipated, and desorption would commence immediately on reversing pressure, and the descending desorption scanning curve would head for the lower hysteresis closure point. This is similar to what was observed for the real sample for scanning curves turning around at relative pressures higher than the kink in the adsorption boundary curve. The narrow, rather than non-existent, hysteresis that was found for scanning curves turning around above and below the kink in the boundary adsorption curve for the real sample are probably due to the much wider distribution in pore

sizes, and deviation from perfect cylindrical geometry, that arises in real materials, in contrast to the abstract model in Figure 12.

The NMR cryoporometry scanning curve data are also consistent with the pore network model shown in Figure 12. If the model were to start with imbibed probe fluid completely frozen, then melting would commence from a cylindrical sleeve-shaped meniscus at the boundary between the non-freezing surface layer and the frozen bulk in the smallest through pore. Once this had melted, hemispherical menisci would be formed at the junction of the smallest through pore and the neighbouring medium-sized pores. These medium sized pores could then melt via these hemispherical menisci. If the melting process was halted with the smallest and medium-sized pores molten but the largest pores remaining frozen then, when the temperature decrease was initiated, freezing could recommence from the hemispherical menisci left at the boundaries between the medium-sized and largest pores. Hence, the melting and freezing of the probe fluid in the medium-sized pores would both occur via hemispherical menisci, and there would be expected to be no hysteresis. In contrast, once the temperature had dropped low enough for the smallest pores to melt this would occur via a hemispherical meniscus, instead of the cylindrical sleeve-shape during melting, and thus hysteresis would be anticipated. Therefore, the medium sized pores would freeze and melt with little or no hysteresis, while hysteresis would be expected between the freezing and melting of the smallest pores. This pattern is similar to what was seen in the experiment, whereby the initial part of the freezing scanning curve had very little hysteresis but this widened substantially at lower temperatures as the smallest pores began to freeze. It was noted above that the melting point depression was half that of the freezing point depression at the lower melting temperature of 267 K, and this factor difference is that was predicted for through cylindrical pores by Petrov and Furo[44].

It is noted that the diagram in Figure 12 is a model structure, and, thus, only represents the features of the network architecture necessary to explain the aforementioned experimental results, and is, thence, as a model, not meant to capture the full complexity of the network.

Figure 12. (a) Schematic diagram of proposed model for pore network (black) of the silica-alumina catalyst, and (b) proposed model for mercury entrapment (grey) in the macropores seen in the CXT images. The rectangles represent through macro- and meso-pores, and the small triangles represent dead-ended micropores formed by surface roughness in the macroporosity.

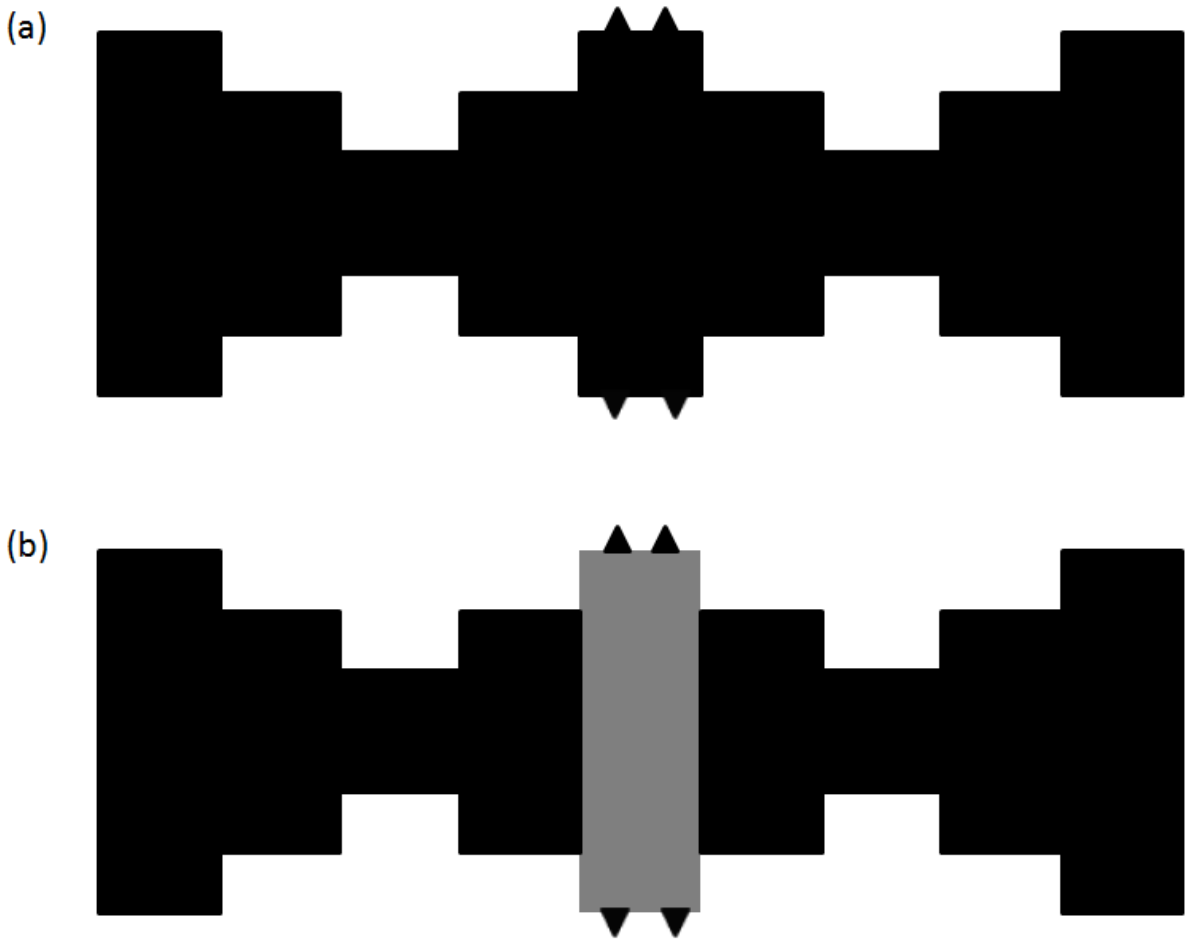

6. CONCLUSIONS

A new method for assessing pore inter-connectivity, employing the recently discovered differential adsorbate-wetting effect, has been demonstrated. Mercury DSC thermoporometry and CXT have shown that mercury only becomes entrapped in the macroporosity of a silica-alumina catalyst. It has been seen that nitrogen is wetting of new mercury surfaces created by entrapment, while argon is not. This difference in wetting between adsorbates leads to a difference in their capillary condensation behaviour following mercury entrapment. This difference allows the sub-set of mesoporosity ‘side-roads’ that directly adjoins the macropore ‘motorways’ to be identified and the specific pore size distribution for this sub-set to be obtained. The basic structural model for the pore network architecture of the pellet has been

confirmed from gas sorption scanning curves and NMR cryoporometry data using technique-specific physical effects often thought as hindering data interpretation, rather than expanding it. It has been shown that the pore network structure is hierarchical with, progressively, smaller pores leading off larger pores, much like the blood circulation network, of larger arteries leading to smaller arterioles, leading to finer capillaries, within animal bodies.

REFERENCES

(1) Schacht, S.; Janicke, M.; Schüth. Modeling X-ray patterns and TEM images of MCM-41. *Micropor. Mesopor. Mater.* **1998**, *22*, 485.

(2) Rigby, S.P.; Beanlands, K.; Evbuomwan, I.O; Watt-Smith, M.J.; Edler, K.J.;Fletcher, R.S. Nanocasting of novel, designer-structured catalyst supports. *Chem. Engng Sci.* **2004**, *59*, 5113.

(3) Yu, P..: Zhao, Y.; Li, Y.; Zhang, Q. Controllable growth of polyaniline nanowire arrays on hierarchical macro/mesoporous graphene foams for high-performance flexible supercapacitors. *Appl Surf Sci* **2017**, *393*, 37.

(4) Lai, W.-F., Susha, A.S.; Rogach, A.L. Multicompartment Microgel Beads for Co-Delivery of Multiple Drugs at Individual Release Rates. *ACS Appl Mater Inter* **2016**, *8*, 18027.

(5) Śrębowata, A.; Tarach, K.; Girman, V.; Góra-Marek, K. Catalytic removal of trichloroethylene from water over palladium loaded microporous and hierarchical zeolites. *Appl. Catal B-Environ* **2016**, *181*, 550.

(6) Fang, C.; Shi, L.; Li, H.; Huang, L.; Zhang, J.; Zhang D. Creating hierarchically macro-/mesoporous Sn/CeO2 for the selective catalytic reduction of NO with NH_3. *RSC Adv*. **2016**, *6*, 78727.

(7) Wen, X.; Zhang, D.; Yan, T.; Zhang, J.; Shi, L. Three-dimensional graphene-based hierarchically porous carbon composites prepared by a dual-template strategy for capacitive deionization. *J. Mater. Chem.* A **2013**, *1*, 12334.

(8) Wen, X.; Zhang, D.; Shi, L.; Yan, T.; Wang, H.; Zhang, J. Three-dimensional hierarchical porous carbon with a bimodal pore arrangement for capacitive deionization. *J. Mater. Chem.* **2012**, *22*, 23835.

(9) Prachayawarakorn, S., Mann, R. Effects of pore assembly architecture on catalyst particle tortuosity and reaction effectiveness. *Catal. Today* **2007**, *128*, 88.

(10) Gheorghiu, S.; Coppens, M.O. Optimal bimodal pore networks for heterogeneous catalysis. *Chem. Engng Sci.* **2004**, 50, 812.

(11) Mann, R. Catalyst deactivation by coke deposition: Approaches based on interactions of coke laydown with pore structure. *Catal. Today* **1997**, *37*, 331.

(12) Koster, A.J.; Ziese, U.; Verklejj, A.J.; Janssen, A.H.; De Jong, K.P. Three-dimensional transmission electron microscopy: a novel imaging and characterization technique with nanometre scale resolution for materials science, *J. Phys. Chem. B* **2000**, *104*, 9368.

(13) Holzer, L.; Indutnyi, F.; Gasser, P.H.; Munch, B.; Wegmann, M. Three-dimensional analysis of porous BaTiO3 ceramics using FIB nanotomography, *Journal of Microscopy* **2004**, *216*, 84.

(14) Rigby, S.P.; Hasan; M.,Hitchcock, I;. Fletcher, R.S. Detection of the delayed condensation effect and determination of its impact on the accuracy of gas adsorption pore size distributions. *Colloids Surf. A: Physiochem. Eng. Aspects* **2017**, *517*, 33.

(15) Hyväluoma, J.; Raiskinmäki, P.; Jäsberg, A.; Koponen, A.; Kataja, M.; Timonen J., Evaluation of a lattice-Boltzmann method for mercury intrusion porosimetry simulations, *Future Generations Computer Sys*tems **2004**, *20*, 1003.

(16) Nepryahin, A.; Fletcher, R.S.; Holt, E.M.; Rigby, S.P. Structure-transport relationships in disordered solids using integrated rate of gas sorption and mercury porosimetry, *Chem. Engng Sci.* 2**016**, *152*, 663.

(17) Seaton, N. Determination of the connectivity of porous solids from nitrogen sorption measurements. *Chem. Engng Sci.* **1991**, *46*, 1895.

(18) Hollewand, M.P.; Gladden, L.F., Heterogeneities in structure and diffusion within porous catalyst support pellets observed by NMR imaging, *J. Catal.* **1993**, 144, 254.

(19) Hollewand, M.P; Gladden, L.F., Transport heterogeneity in porous pellets-II. NMR imaging studies under transient and steady-state conditions, *Chem. Engng Sci.* **1995**, *50*, 327.

(20) Liu, H.L.; Zhang, L.; Seaton, N.A. Analysis of sorption hysteresis in mesoporous solids using a network model. *J. Colloid Interface Sci.* **1993**, *156*, 285.

(21) Matthews, G.P.; Ridgway, C.J.: Spearing M.C. Void space modeling of mercury intrusion hysteresis in sandstone, paper coating and other porous media, *J. Colloid Interface Sci.* **1995**, *171*, 8.

(22) Tsakiroglou C.D., Payatakes A.C. Effects of pore-size correlations on mercury porosimetry curves. *Journal of Colloid and Interface Science* **1991**, *146*, 479.

(23) Tsakiroglou, C.D.; Burganos, V.N.; Jacobsen, J. Pore structure analysis by using nitrogen sorption and mercury intrusion data, *AIChEJ*. **2004**, *50*, 489.

(24) Rigby, S.P.; Fletcher, R.S.; Riley, S.N. Characterisation of porous solids using integrated nitrogen sorption and mercury porosimetry. *Chem. Engng Sci.* **2004**, *59*, 41.

(25) Rigby S.P.; Watt-Smith M.J.; Fletcher R.S. Simultaneous determination of the pore-length distribution and pore connectivity for porous catalyst supports using integrated nitrogen sorption and mercury porosimetry. *J. Catal.* **2004**, *227*, 68.

(26) Thommes, M.; Smarsly, B.; Groenewolt, M.; Ravikovitch, P.I.; Neimark, A.V. Adsorption hysteresis of nitrogen and argon in pore networks and characterization of novel micro- and mesoporous silicas. *Langmuir* **2006**, *22*, 756.

(27) LopezRamon, M.V.; Jagiello, J.; Bandosz, T.J.; Seaton, N.A. Determination of the pore size distribution and network connectivity in microporous solids by adsorption measurements and Monte Carlo simulation. *Langmuir* **1997**, *13*, 4435.

(28) Matadamas, J.; Alferez, R.; Lopez, R.; Roman, G.; Kornhauser, I.; Rojas, F. Advanced and delayed filling or emptying of pore entities by vapour sorption or liquid intrusion in simulated porous networks. *Colloids Surf. A: Physiochem. Eng. Aspects* **2016**, *496*, 39.

(29) Wardlaw N.C.; McKellar M. Mercury porosimetry and the interpretation of pore geometry in sedimentary rocks and artificial models. *Powder Technol.* **1981**, *29*, 127.

(30) Perkins, E.L.; Lowe, J.P.; Edler, K.J.; Tanko, N.; Rigby, S.P. Determination of the percolation properties and pore connectivity for mesoporous solids using NMR cryodiffusometry, *Chem. Engng Sci.* **2008**, *63*, 1929.

(31) Washburn, E.W. The dynamics of capillary flow. *Phys. Rev.* **1921,** *17*, 273.

(32) Kloubek, J. Hysteresis in porosimetry, *Powder Technol.* **1981**, *29*, 63.

(33) Rigby, S.P. New methodologies in mercury porosimetry. *Stud. Surf. Sci. Catal.* **2002**, *144*, 185.

(34) Liabastre, A.A.; Orr, C. Evaluation of pore structure by mercury penetration. *J. Colloid Interface Sci.***1978**, *64***,** 1.

(35) Rigby, S.P.; Chigada, P.I. MF-DFT and experimental investigations of the origins of hysteresis in mercury porosimetry of silica materials, *Langmuir* **2009**, *26*, 241.

(36) Mitchell, J.; Webber, J.B.W.; Strange, J. Nuclear magnetic resonance cryoporometry. *Physics Reports* **2008**, *461*, 1.

(37) Bafarawa, B.; Nepryahin, A.;, Ji, L.; Holt, E.M.; Wang, J.; Rigby, S.P. Combining mercury thermoporometry with integrated gas sorption and mercury porosimetry to improve accuracy of pore-size distributions for disordered solids, *J. Colloid Interface Sci*. **2014**, *426*, 72.

(38) Borisov, B.F.; Charnaya, E.V.; Plotnikov, P.G.; Hoffmann, W.D.; Michel, D.; Kumzerov, Y.A.; Tien, C.; Wur, C.C.. Solidification and melting of mercury in a porous glass as studied by NMR and acoustic techniques. *Phys. Rev. B* **1998**, *58*, 5329.

(39) Hitchcock, I.; Malik, S.; Holt, E.M.; Fletcher, R.S.; Rigby, S.P. (2014). On the Impact of Chemical Heterogeneity on the Accuracy of Pore Size Distributions in Disordered Solids, *J. Phys. Chem. C* **2014**, *118*, 20627.

(40) McMillan, W.G. Multilayer Adsorption on Composite Surfaces. *J. Chem. Phys.* **1947**, *15*, 390.

(41) Mahnke, M.; Mögel, H.J. Fractal Analysis of Physical Adsorption on Material Surfaces. *Colloids Surf., A* **2003**, *216*, 215.

(42) Cohan, L.H. Sorption Hysteresis and the Vapor Pressure of Concave Surfaces. *J. Am. Chem. Soc*. **1938**, *60*, 433.

(43) Giesche, H. Mercury porosimetry: A general (practical) overview. *Part. Part. Sys. Charac.* **2006**, *23*, 9.

(44) Petrov, O., Furó, I. Curvature-dependent metastability of the solid phase and the freezing-melting hysteresis in pores. *Phys. Rev. E* **2006**, *73*, 011608.